An Adaptive Carrier Frequency Optimization Method for Harmonic Energy Unbalance Minimization in a Cascaded H-Bridge-Based Active Power Filter

Zezhou Yang, *Student Member, IEEE*, Jianjun Sun, *Member, IEEE*, Shangsheng Li, *Member, IEEE*,
Meng Huang, *Member, IEEE*, Xiaoming Zha, *Member, IEEE*, and Yi Tang, *Member, IEEE*

***Abstract*—Cascaded H-bridge (CHB) based active power filters (APF) can compensate high-order harmonics in medium and high-voltage systems with relatively low switching frequency. This paper reveals that a severe dc capacitor energy unbalance can be induced by harmonic energy exchange if the frequency of APF output current coincides with the switching harmonic frequency of CHB cells. The mechanism of harmonic energy exchange is analyzed, and it is found that the dc capacitor energy unbalance is essentially affected by the carrier frequency of CHB. A noninteger ratio carrier frequency can be adopted to avoid the divergence of dc voltage, but there is still a significant low-frequency ripple on the dc voltage. This paper proposes an adaptive carrier frequency optimization method. By predicting the dc voltage ripple amplitude under different carrier frequencies, this method can adaptively select the optimal carrier frequency to minimize the dc voltage ripple. The proposed method is also proved to be robust against system parameter variations, and it can be implemented by a practical and simple linear computation method. Results obtained from simulation, experimental prototype, and field test are finally presented to verify the proposed adaptive carrier frequency optimization method.**

***Index Terms*—Carrier phase-shifted modulation, cascaded H-bridge (CHB) active power filters (APF), dc voltage ripple, dc voltage unbalance, harmonic energy.**

I. INTRODUCTION

THE increasing use of high power and high voltage nonlinear loads has introduced severe harmonic pollutions in modern electric distribution systems. Using passive filters is a feasible way to mitigate these harmonics, but these devices typically have low compensation ratings, high risk of resonance, inflexibilities in terms of control and harmonic compensation, which may greatly limit their performance when used for power quality improvement. Alternatively, medium and high voltage active power filter (APF) is a promising application for harmonic compensation. In general, there are three categories of topologies for implementing a medium or high voltage APF, i.e., low-voltage APF with step-up transformer [1], [2], LC coupled hybrid APF [3]–[5], and cascaded H-bridge (CHB) based APF. Among these topologies, CHB-based APF has the advantages of smaller size, lower loss, higher output current quality, and higher equivalent switching frequency with carrier phase-shifted modulation (CPS-PWM). High equivalent switching frequency can effectively reduce the electromagnetic interference of APF and make it possible to compensate high-order harmonics (over 17th) with relatively low switching frequency (0.5–1 kHz) [6], [7]. Thus, CHB-based APF (as Fig. 2) has become the most preferred harmonic compensator in medium and high voltage systems [6]–[11].

For CHB-based APF, it is critical to maintain the dc voltage of each H-bridge cell at rated value to ensure proper control and operation of the overall system, and this topic has recently attracted a lot of research attentions [12]–[15]. However, the individual dc voltage unbalance problem, which is also one of the key issues in CHB-based APF, has not been well studied in existing literatures. Generally, individual dc voltage unbalance in a CHB converter can be caused by two reasons, i.e., uneven power loss and cell energy exchange. Uneven power loss is mainly due to the parameter tolerance of passive and active components in CHB and could be mitigated by improving device consistency, thermal design, etc. Cell energy exchange will be much more complicated and is related to control, modulation, operating condition, and many other factors, such as uneven dc power supply [16], uneven firing delay, the difference of modulation carriers [17], the residual switching harmonic voltages induced by nonideal operating conditions of CPS-PWM [18], [19].

This paper further studies the dc voltage unbalance caused by cell energy exchange and reveals that when a CPS-modulated CHB converter is adopted for APF applications, the compensated harmonic current could be coupled with the switching harmonic voltages of individual H-bridge cells, leading to a significant harmonic energy unbalance (HEU) phenomenon and dc voltage unbalance. It should be noted that this HEU is different with the capacitor voltage variation caused by the coupling of fundamental components in [20]. Without proper suppression, this HEU would result in the divergence of dc

Manuscript received August 17, 2016; revised January 26, 2017; accepted March 1, 2017. Date of publication March 7, 2017; date of current version November 2, 2017. This work was supported by the National Natural Science Foundation of China under Grant 51277137. Recommended for publication by Associate Editor H.-P. Nee. *(Corresponding author: J. Sun.)*

Z. Yang, J. Sun, S. Li, M. Huang, and X. Zha are with the School of Electrical Engineering, Wuhan University, Wuhan 430072, China (e-mail: zezhouyang@whu.edu.cn; jjsun@whu.edu.cn; l.ss007@163.com; meng.huang@whu.edu.cn; xmzha@whu.edu.cn).

Y. Tang is with the School of Electrical and Electronic Engineering, Nanyang Technological University, Singapore, 639798 (e-mail: yitang@ntu.edu.sg).

Color versions of one or more of the figures in this paper are available online at http://ieeexplore.ieee.org.

Digital Object Identifier 10.1109/TPEL.2017.2679028

capacitor voltages or even unstable operation of the entire CHB system.

Existing individual dc voltage balancing strategies can be typically classified into two categories, depending on whether the dc voltage balancing is implemented in the control loop or the modulation process. For the first category, an additional voltage balancing controller is required in the control loop of each cell to regulate respective fundamental modulation reference and achieve voltage balancing [16], [21]–[23]. However, regulation of the modulation reference may lead to nonideal switching harmonic elimination in the overall output voltage [24]. Moreover, the fundamental output current required for voltage balancing does not always exist in APF applications. Hence, this category of balancing control strategies is not suitable to cope with the HEU in the CHB-based APF. The second category of individual dc voltage balancing control is based on modification of modulation, which can avoid the drawback of adding additional voltage balancing controllers. Carrier rotation [17] is a widely used modulation-based method, but the long cycle time of carrier rotation leads to a high-amplitude low-frequency ripple on the dc voltage. A group of sorting methods (a.k.a. module selection methods) have been proposed to achieve a better performance than carrier rotation, such as the predictive sorting algorithm [25], [26], the distributed commutations modulation [27], [28], the improved phase disposition PWM [29], and the single-bit information-based modulation [30]. According to capacitor voltages and phase current direction, these sorting methods selectively distribute PWM pulse or carrier to each cell to charge or discharge capacitors and keep energy balance. However, the complicated sorting algorithm and all PWM pulses generation are executed in a central controller, which is computation-intensive and prone to single-point failure. Moreover, it leads to an uncertain computation delay and makes it difficult to be extended for higher voltage higher level applications. Reference [18] proposed a noninteger ratio carrier frequency modulation method to solve the nonideal CPS-PWM-induced harmonic energy exchange problem, and a similar method is also analyzed for modular multilevel converters in [19]. Nevertheless, two drawbacks make this noninteger ratio carrier frequency modulation method not suitable for CHB-based APFs. First, the output harmonics of CHB-based APFs are load-dependent and have much higher amplitudes. This makes the operation of CHB converters more complicated, which is not considered in the design. Moreover, significant low-frequency ripples may appear in the dc voltages if the noninteger ratio carrier frequency is not properly chosen, which may degrade the output current regulation and the lifetime of the dc capacitors. It should be noted that the well-known optimal selected harmonic elimination PWM [31] that aims at eliminating selected harmonics in the overall output of a CHB converter cannot be used to solve the HEU discussed in this paper, because HEU is essentially an internal harmonic problem caused by the coupling of harmonic voltage and current within the CHB converter. Such an issue still exists in a CHB-based APF system even when the corresponding harmonics are perfectly eliminated at the point of common coupling (PCC).

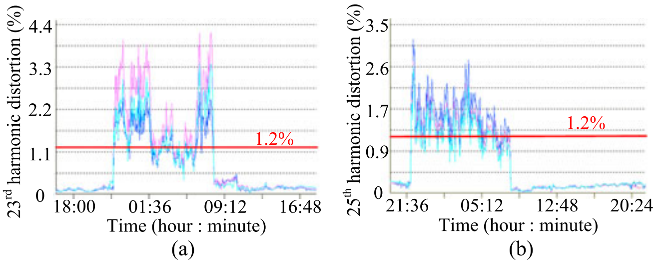

Fig. 1. Measured daily harmonic distortion curves at a 110 kV bus in Central China. (a): 23rd harmonic; (b): 25th harmonic.

This paper analyzes the mechanism of the HEU phenomenon in a CHB-based shunt APF. It is found that HEU is closely related to the carrier frequency of CHB cells. Then, an adaptive carrier frequency optimization (ACFO) method is proposed to suppress the HEU among different cells in the CHB. Based on the calculation of harmonic energy exchange, the possible dc voltage ripple under different carrier frequencies is predicted adaptively for any output harmonic currents, and the optimal carrier frequency that leads to a minimized dc voltage ripple amplitude is selected. Moreover, to reduce the complexity of calculation, a simplified implementation of the ACFO method is proposed for engineering applications. The nonlinear calculation and optimization of the original method are simplified into an adaptive linear combination of several carrier frequency shifting factors, which are obtained offline and stored in the controller as a simple lookup table. The proposed ACFO method retains all the advantages of CPS-PWM, such as high equivalent switching frequency, great extensibility, and easy implementation. Since the ACFO method not only avoids the divergence of dc voltages but also minimizes dc voltage ripples, the quality of the output current in the CHB-based APF can be greatly improved, and the lifetime of the cell capacitors can be extended as well. Finally, the ACFO method is verified by simulation, experimental prototype, and field test.

II. HEU PHENOMENON IN CHB-BASED APF

A. *High-Order Harmonics in Medium Voltage Systems*

Electric arc furnace (usually 35 kV), medium and high voltage rectifier (10 – 110 kV) and other high-power nonlinear loads would generate wideband harmonic pollutions. Due to the high power rating, such harmonics can cause severe power quality issues in electric distribution systems. Fig. 1 presents an example of high-order harmonic pollution monitored in a 110 kV public power grid in Central China. During the night, the 23rd and 25th harmonics were seriously out of 1.2% limit specified by [32], because a nearby smelting plant works mainly in the night due to lower electricity tariff. This smelting plant is equipped with a static VAR compensator for reactive power and low-order harmonic compensation, while high-order harmonics are out of control and may penetrate through a 35 kV/110 kV distribution transformer into the 110 kV public power grid, causing serious power quality issues to other users. Many similar examples can be found in practical and industrial applications, which indicate that with the development of modern power system and loads, it is imperative to adopt more advanced harmonic compensation techniques, e.g., CHB-based APF, to eliminate high order harmonics in medium and high voltage systems.

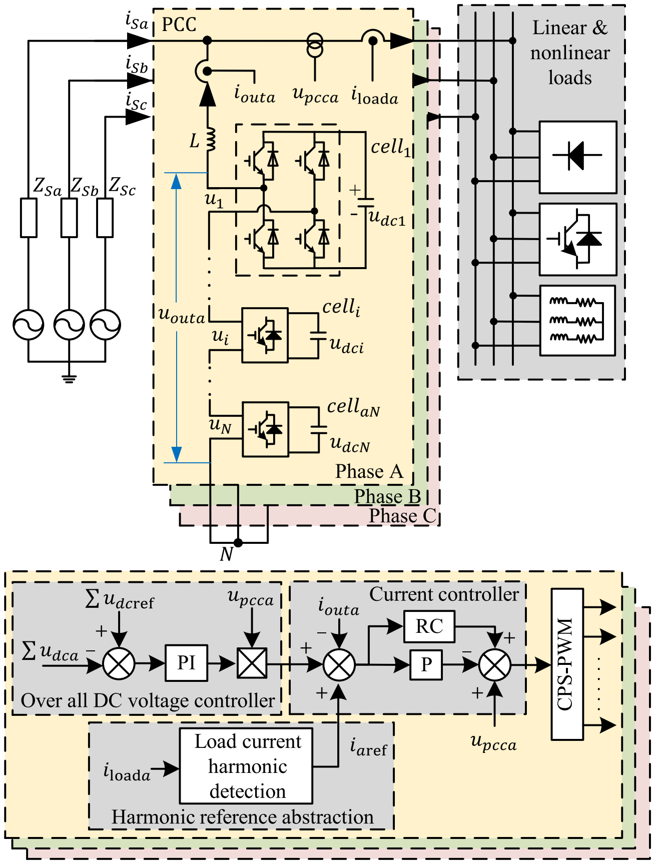

Fig. 2. Schematic diagram of the topology and controller of CHB-based APF.

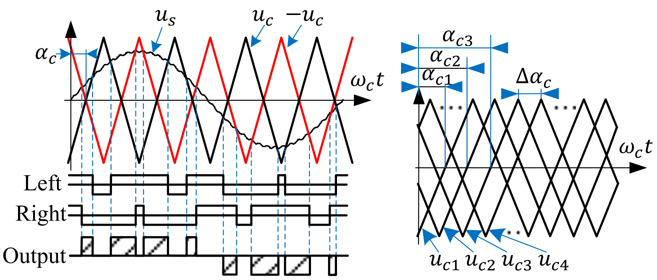

(a) (b)

Fig. 3. Schematic diagram of the CPS-PWM. (a):Unipolar double frequency modulation for every H-bridge cell; (b): Phase-shifted carriers of different cells (only the carrier of the left leg is shown).

B. Introduction of CHB-Based APF

Fig. 2 shows the topology and control schemes of a CHB-based shunt APF. The current reference extraction algorithm is based on the discrete Fourier transform analysis of the load current. A proportional (P) controller plus repetitive controller is adopted in the inner current control loop, and a proportional integral controller is adopted in the overall voltage control loop. Since the harmonic voltages generated by each individual H-bridge cells in each phase are independent with the operation of other two phases, only a single-phase system is studied in this paper for simplicity.

The unipolar double frequency triangle-carrier modulation with natural sampling, shown in Fig. 3(a), is applied to each H-bridge cell. The π/N CPS-PWM shown in Fig. 3(b) is applied to each phase of the CHB. Denote the modulation reference of all the cascaded cells as u_s, and the carrier of the ith cell as u_{ci}

$$\begin{cases} u_s = U_s\sin(\omega_s t+\alpha_s)+\sum\limits_{h>1} U_h\sin(\omega_h t+\alpha_h) \\ u_{ci} = \begin{cases} -[\omega_c t+\alpha_{ci}-2\pi(k+1)]2U_c/\pi-U_c, \\ \qquad 2\pi k+\pi \le \omega_c t \le 2\pi(k+1) \\ (\omega_c t+\alpha_{ci}-2\pi k)2U_c/\pi-U_c, \\ \qquad 2\pi k \le \omega_c t \le 2\pi k+\pi \end{cases} \end{cases} \tag{1}$$

Where, U_s, ω_s (corresponding frequency f_s), and α_s are the amplitude, angular frequency, and initial phase of the fundamental component in the modulation reference, respectively; U_h, ω_h (corresponding frequency f_h), and α_h are the amplitude, angular frequency, and initial phase of the hth harmonic component in the modulation reference, respectively; U_c, T_C (corresponding frequency f_c), and α_{ci} are the amplitude, period, and initial phase of the carrier waveform for the left leg the ith cell, respectively; k is an integer. Due to multilevel output, the inductor filter of CHB converter is very small, and its harmonic voltage drop is far lower than the grid voltage. Therefore, the harmonic component can be ignored as compared to the fundamental component in the modulation reference. In this case, u_s can be simplified as (2), where M is the modulation index and $U_{\mathrm{dc}i}$ is the dc voltage of ith cell.

$$u_s = U_s\sin(\omega_s t+\alpha_s) = MU_{\mathrm{dc}i}\sin(\omega_s t+\alpha_s). \tag{2}$$

Based on the dual Fourier analysis theory [22], the output voltage of each cell is u_i as

$$u_i = \underbrace{MU_{\mathrm{dci}}\cos(\omega_s t+\alpha_s)}_{\text{fundamental part}} + \underbrace{\frac{2}{\pi}U_{\mathrm{dci}}\sum_{m=1}^{\infty}\sum_{k=-\infty}^{\infty}\frac{1}{m}\cos\left[(m+k+1)\pi\right]J_k\left(mM\pi\right) \cdot\cos\left[2\mathrm{m}\left(\omega_\mathrm{c}\mathrm{t}+\alpha_\mathrm{ci}\right)+\mathrm{k}(\omega_\mathrm{s}\mathrm{t}+\alpha_\mathrm{s})\right]}_{\text{switching harmonic part}} \tag{3}$$

where J_k is a kth-order first kind Bessel function; $m = 1, 2, 3\cdots$ is the order of harmonic cluster; $k = \pm1, \pm3, \pm5\cdots$ is the order of side-band harmonic in one cluster. Equation (3) shows that the output PWM waveform of each cell is composed of a fundamental component corresponding to the modulation reference and a switching harmonic component, which includes multiple clusters of harmonics at the frequency of $(2mf_c+kf_s)$. For convenience, the harmonic component $@(2m\omega_c+k\omega_s)$ in u_i can also be written as a vector form in the synchronous rotating frame as in (4), where a_{hi} is the amplitude of the harmonic vector, and $\theta_{hi} = (2m\alpha_{ci}+k\alpha_s)$ is the phase of the harmonic vector. It should be noted that a_{hi} does not change with i when the dc voltages are balanced, the harmonic component $@(2m\omega_c+k\omega_s)$ in the overall output voltage in one phase of the CHB is

$$U_{hi}@(2m\omega_c+k\omega_s) = \underbrace{\frac{2}{\pi m}U_{\mathrm{dc}i}J_k(mM\pi)\cos\left[(m+k+1)\,\pi\right]}_{a_{hi}}\underbrace{e^{j(2m\ \alpha_{ci}+k\ \alpha_s)}}_{\angle\theta_{hi}} \tag{4}$$

$$U_{\mathrm{out}}@(2m\omega_c+k\omega_s) = a_h\sum_{i=1}^{N}e^{j\theta_{hi}}. \tag{5}$$

For the CPS-PWM technique, all cells in the same phase share the same modulation reference, while carrier phase α_{ci} of each cell is shifted by an angle of $\Delta\alpha = \pi/N$, leading to a mutual phase difference of $2m\Delta\alpha$ in θ_{hi}. Specifically, for the harmonic cluster $m \neq jN$, $j = 1, 2, 3\cdots$, all the *N* harmonic vectors are equally distributed in one cycle. Therefore, the sum of harmonic vectors is zero and the switching harmonic $@(2m\omega_c + k\omega_s)$ is counteracted in the overall output voltage. For the harmonic cluster $m = jN$, all the *N* harmonic vectors are in phase. Thus, the total harmonic in the overall output voltage is the linear superposition of the amplitude of *N* vectors. This explains why the equivalent switching frequency of CHB is multiplied to $2Nf_c$.

Although the switching harmonics in the first *N*-1 clusters are all counteracted in the overall output voltage, they still remain in the output voltage of individual cells with different phases. This is the root cause of unbalanced harmonic energy exchange, and its mechanism will be analyzed in the following section.

C. Harmonic Energy Exchange and HEU Phenomenon

As introduced above, the CHB-based APF should be able to compensate high-order harmonics (over 17th) in medium and high-voltage systems. For high-voltage and high-power semiconductor switches, the device switching frequency is commonly limited to several hundred hertz [28], [33], which is exactly in the band of harmonic current that needs to be compensated by the APF. For example, when a 600-Hz carrier is used in a ten-cell CHB-based APF to reach an equivalent switching frequency of 12 kHz, the first cluster of switching harmonics in individual cells is located at (1200 ± 50), (1200 ± 150), and (1200 ± 250) Hz, which overlap with 19th, 21st, 23rd, 25th, 27th, and 29th harmonic currents in the CHB-based APF.

When the frequency of the output current coincides with the switching harmonic frequency of H-bridge cells, different cells in the same CHB-chain would exchange power at the harmonic frequency. Since the phases of the switching harmonics are symmetrically distributed in one cycle and all cells share the same current, the power factor at the harmonic frequency varies from cell to cell. For example, for a three-cell-cascaded APF, when the output current includes harmonic component $I_h@(2f_c - f_s)$, the vector diagrams of this current and switching harmonic voltages of all cells at the same frequency are shown in Fig. 4. Although the sum of the three switching harmonic voltages is zero, the harmonic power factors are different. Thus, some of the cells keep charging while the others keep discharging, resulting in the divergence of dc voltages and fault tripping.

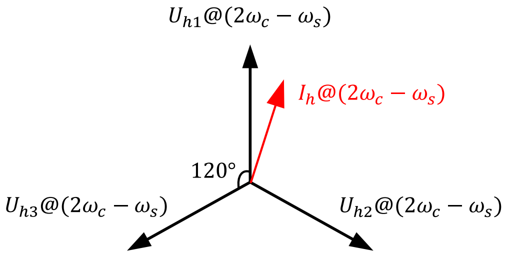

Fig. 4. Coupling of harmonic current and switching harmonic voltages of different cells.

TABLE I
CALCULATION EXAMPLES OF HARMONIC POWER UNBALANCE IN A THREE-CELL- CASCADED APF

Harmonic order	current $(\mathrm{A})_{\mathrm{rms}}$	Voltage $(\mathrm{V})_{\mathrm{rms}}$	Active power (W)		
			Cell 1	Cell 2	Cell 3
27th	5	10.0	50.2	–25.1	–25.1
25th	5	214.9	1074.6	–537.3	–537.3
23rd	5	214.9	1074.6	–537.3	–537.3
19th	5	10.0	50.2	–25.1	–25.1
17th	5	0.43	2.1	–1.1	–1.1
13th	5	1.59×10^{-4}	7.9×10^{-4}	-4×10^{-4}	-4×10^{-4}
11th	5	1.72×10^{-6}	~	~	~
Total active harmonic power			2251.7	–1125.9	–1125.9

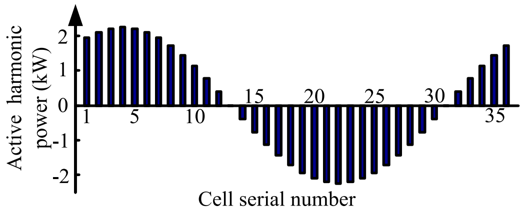

Fig. 5. Active harmonic power of each cell in a 36-cell-CHB-based APF which output 11th –27th harmonic currents.

To manifest the magnitude of HEU intuitively, a calculation example based on a single phase three-cell-casecaded APF is presented as following. Assuming that $U_{\mathrm{dc}} = 1000$ V; $M = 0.82$; $f_c = 600$ Hz; the carrier initial phase of *cell* 1 is zero; the frequency of the grid is 50 Hz; the compensation harmonic currents are all 5 A (rms); and the initial phases of all currents are zero. Thus, the active power of the three cells at different harmonic frequencies is shown in Table I. The harmonic voltage in Table I is calculated by (4). In this example, the unbalanced active harmonic power exchange can be higher than 2 kW, which would cause a fast divergence of dc voltages. Assuming the dc capacitor is 4500 μF, the dc voltage variation would exceed 40% of the nominal value within 1 s.

In order to show the characteristics of the HEU more comprehensively, another example based on a 36-cell-cascaded APF is presented. The parameters are the same with those used in the previous example except that the initial phases of harmonic currents are all shifted by 30°. The total unbalanced harmonic power of each cell is shown in Fig. 5.

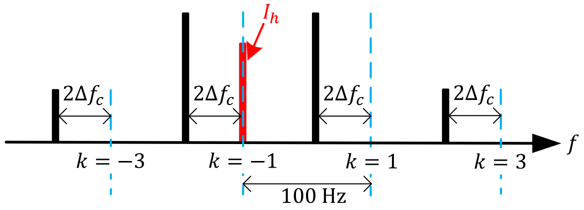

Fig. 6. Spectrum schematic of the switching harmonics before and after carrier frequency optimization.

The sine shape in Fig. 5 is explained by the symmetrical distribution of the switching harmonic phases in CPS-PWM. It is worth noting that the sum of the harmonic power of all cells is zero, which means that HEU is caused by internal power exchange between different cells in the same phase of CHB. As evidenced by these examples, HEU can cause severe dc voltage unbalance problems and must be suppressed with proper control.

If the carrier frequency is multiple of the fundamental frequency. For instance, if the carrier frequency f_c is changed to 900 Hz, the dominant switching harmonics will be surrounding the 36th ($2f_c/50 = 36$) harmonic. In this case, the CHB-based APF still faces the same HEU issue when it is used to compensate 31st, 33rd, 35th, 37th, 39th, and 41st harmonic currents, which fall in the scope specified in the IEC6100-3-6 standard [32]. Further increasing the carrier frequency will lead to excess switching losses and may not be a viable solution for high power APF applications.

Generally, the source current harmonic detection in an APF system is simply realized by subtracting the fundamental component from the measured nonlinear load current. As long as the nonlinear load current does not contain the harmonic components that overlap with the switching harmonic voltages of H-bridge cells, this HEU phenomenon will not happen. Therefore, the HEU can be considered to be irrelevant to the harmonic detection method.

III. ACFO METHOD

From the above analysis, the root cause of HEU-induced dc voltage divergence is due to the coupling between the switching harmonic voltage of CHB cells and the harmonic current of CHB-based APF. Since the output harmonic current of APF is determined by nonlinear loads which in the sense is uncontrollable, the only way to mitigate HEU-induced dc voltage divergence is to change the switching harmonic spectrum of CHB cells. Based on this idea, a carrier frequency optimization method is proposed to properly shift (increase or decrease) the carrier frequency of all cells so that the coupling between harmonic voltage and current in a CHB-based APF can be avoided.

The carrier frequency shift Δf_c should be limited in a certain range. Fig. 6 explains the case when the carrier frequency is shifted by Δf_c. Assume that before shifting, the switching harmonic $@(2f_c - f_s)$ is coupled with I_h; after shifting, their frequencies differ by $2\Delta f_c$. To avoid the harmonic current recoupling with adjacent switching harmonic, $2\Delta f_c$ should be limited within ±100 Hz. Once Δf_c satisfies (6), the dc voltage divergence caused by HEU can be avoided:

$$-50\ \text{Hz} < \Delta f_c < 50\ \text{Hz},\ \Delta f \neq 0. \tag{6}$$

However, if the carrier frequency shift is not wide enough, there will be a low-frequency fluctuating power exchange reflected in the dc voltage of each cell as a low-frequency ripple. Thus, it is necessary to select an optimal Δf_c to minimize the dc voltage ripple.

Assuming that the output harmonic current is

$$i_h = I_h \cos(\omega_h t + \theta_h). \tag{7}$$

Consider i_h is coupled with the switching harmonic at $(2m_h\omega_c + k_h\omega_s)$ before shifting, i.e., $\omega_h = 2m_h\omega_c + k_h\omega_s$. After shifting the carrier frequency by Δf_c, the corresponding switching harmonic component of the ith cell turns into

$$u_{hi} = a_h \cos[(\omega_h + 2\Delta\omega_c)t + 2m_h\alpha_{ci} + k_h\alpha_s]. \tag{8}$$

Therefore the harmonic instantaneous power of the ith cell is

$$\begin{aligned} p_{hi} &= u_{hi} \cdot i_h \\ &= \frac{a_h I_h}{2}\left\{\begin{array}{l}\cos[(2\omega_h + 2\Delta\omega_c)t + 2m_h\alpha_{ci} + k_h\alpha_s + \theta_h] \\ + \cos(2\Delta\omega_c t + 2m_h\alpha_{ci} + k_h\alpha_s - \theta_h)\end{array}\right\}. \end{aligned} \tag{9}$$

Equation (9) indicates that the harmonic instantaneous power includes two components, i.e., a high-frequency component at $(2f_h + 2\Delta f_c)$ and a low-frequency component at $2\Delta f_c$. By integrating (9), the energy exchange of the capacitor is obtained as

$$\begin{aligned} w_{hi} &= \int p_{hi} dt \\ &= \frac{a_h I_h}{2}\left\{\begin{array}{l}\dfrac{\sin[(2\omega_h + 2\Delta\omega_c)t + 2m_h\alpha_{ci} + k_h\alpha_s + \theta_h]}{2\omega_h + 2\Delta\omega_c} \\ + \dfrac{\sin(2\Delta\omega_c t + 2m_h\alpha_{ci} + k_h\alpha_s - \theta_h)}{2\Delta\omega_c}\end{array}\right\}. \end{aligned} \tag{10}$$

Equation (10) indicates that the low-frequency component dominates the energy exchange and energy unbalance as the amplitude is much higher than the high-frequency component. It is also observed from (10) that the amplitude of the energy exchange is inversely proportional to $|\Delta f_c|$. In order to minimize the dc voltage ripple, $|\Delta f_c|$ should be as large as possible within the restriction of (6). But when Δf_c is close to -50 Hz, the switching harmonic at $(\omega_h + 2\omega_s)$ is close to the frequency of the harmonic current, which will also cause a high-amplitude low-frequency dc voltage ripple. Similarly, when Δf_c is close to 50 Hz, the switching harmonic voltage at $(\omega_h - 2\omega_s)$ is close to the frequency of the harmonic current. Hence, it is necessary to take these three switching harmonics, i.e., $\omega_{\rm h}$ and $\omega_{\rm h} \pm 2\omega_{\rm s}$ into consideration. For other switching harmonics, they are located far away from the harmonic current $i_{\rm h}$ and the coupling effect is negligible. Considering the energy exchange caused by these three switching harmonic voltages at $(\omega_h;\ \omega_h \pm 2\omega_s)$, the approximate value of the total energy exchange in the dc capacitor is obtained as

$$\begin{aligned}\sum w_{hi} &= \frac{a_h I_h}{2}\,\frac{\sin(2\Delta\omega_c t + 2m_h\alpha_{ci} + k_h\alpha_s - \theta_h)}{2\Delta\omega_c}\\ &+\frac{a_{h+2\omega_s} I_h}{2}\,\frac{\sin[2(\Delta\omega_c + \omega_s)t + 2m_h\alpha_{ci} + (k_h{+}2)\,\alpha_s - \theta_h]}{2(\Delta\omega_c + \omega_s)}\\ &+\frac{a_{h-2\omega_s} I_h}{2}\,\frac{\sin[2(\Delta\omega_c - \omega_s)t + 2m_h\alpha_{ci} + (k_h{-}2)\,\alpha_s - \theta_h)}{2(\Delta\omega_c - \omega_s)}.\end{aligned} \tag{11}$$

The worst case happens when the three components in (11) are added at the peak values. Since the amplitude of $\sum w_{hi}$ does not vary with the cell number *i*, the amplitudes of the dc voltage ripples of all cascaded cells are the same. Denote the amplitude of $\sum w_{hi}$ in the worst case as $W_{\max}$, then:

$$W_{\max} = \left|\frac{a_h I_h}{4\Delta\omega_c}\right| + \left|\frac{a_{h+2\omega_s} I_h}{4(\Delta\omega_c + \omega_s)}\right| + \left|\frac{a_{h-2\omega_s} I_h}{4(\Delta\omega_c - \omega_s)}\right|. \tag{12}$$

Denote, the amplitude of dc voltage ripple as $\Delta U_{\mathrm{dcmax}} = U_{\mathrm{dcmax}} - U_{\mathrm{dcmean}}$, where U_{dcmax} is the maximum dc voltage; U_{dcmean} is the mean value (the dc component) of the dc voltage. According to the relationship between the voltage and the stored energy of a capacitor, there is

$$\begin{aligned}&\frac{C}{2}U^2_{\mathrm{dc\,max}} - \frac{C}{2}U^2_{\mathrm{dc\,mean}} = W_{\max}\\ &= \left|\frac{a_h I_h}{4\Delta\omega_c}\right| + \left|\frac{a_{h+2\omega_s} I_h}{4(\Delta\omega_c + \omega_s)}\right| + \left|\frac{a_{h-2\omega_s} I_h}{4(\Delta\omega_c - \omega_s)}\right|.\end{aligned} \tag{13}$$

Substituting the expressions of a_h, $a_{h+2\omega_s}$, $a_{h-2\omega_s}$ into (13),

$$\begin{aligned}C\left(U^2_{\mathrm{dc\,max}} - U^2_{\mathrm{dc\,mean}}\right) &\approx \left|\frac{I_h U_{\mathrm{dc}} J_{k_h}(m_h M\pi)}{\pi\Delta\omega_c}\right|\\ &+ \left|\frac{I_h U_{\mathrm{dc}} J_{k_h+2}(m_h M\pi)}{\pi(\Delta\omega_c + \omega_s)}\right| + \left|\frac{I_h U_{\mathrm{dc}} J_{k_h-2}(m_h M\pi)}{\pi(\Delta\omega_c - \omega_s)}\right|.\end{aligned} \tag{14}$$

The U_{dc} in (14) is the reference value of the dc voltage. Since $U_{\mathrm{dcmean}} \approx U_{\mathrm{dc}}$, $U_{\mathrm{dcmax}} = U_{\mathrm{dcmean}} + \Delta U_{\mathrm{dcmax}}$, and $\Delta U_{\mathrm{dc}} \ll U_{\mathrm{dc}}$, we have

$$\begin{aligned}C\left(U^2_{\mathrm{dc\,max}} - U^2_{\mathrm{dc\,mean}}\right) &= \mathrm{C}(2U_{\mathrm{dc}}\Delta U_{\mathrm{dc\,max}} + \Delta U^2_{\mathrm{dc\,max}})\\ &\approx 2CU_{\mathrm{dc}}\Delta U_{\mathrm{dc\,max}}.\end{aligned} \tag{15}$$

Combining (14) and (15) and normalizing them by using U_{dc}, the amplitude of dc voltage ripple is obtained as

$$\begin{aligned}&\Delta U_{\mathrm{dc\,max}} \approx\\ &\frac{I_h}{2\pi C}\left(\left|\frac{J_{k_h}(m_h M\pi)}{\Delta\omega_c}\right| + \left|\frac{J_{k_h+2}(m_h M\pi)}{\Delta\omega_c + \omega_s}\right| + \left|\frac{J_{k_h-2}(m_h M\pi)}{\Delta\omega_c - \omega_s}\right|\right).\end{aligned} \tag{16}$$

According to (16) the curve of the dc voltage ripple amplitude $\Delta U_{\mathrm{dcmax}}$ versus Δf_c can be obtained. For example, assume that $I_h = 10$ A, $C = 4500$ μF, $M = 0.75$. For output current with frequency of $f_h = 2f_c - f_s$, the $\Delta U_{\mathrm{dcmax}}$–$\Delta f_c$ curve is shown in Fig. 7(a), where it shows that the optimal frequency shift $\Delta f_{c-\mathrm{optimal}}$ is 30 Hz, which gives the minimum $\Delta U_{\mathrm{dcmax}}$. Similarly for $f_h = 2f_c + f_s$, the curve is shown in Fig. 7(b) and the optimal frequency shift is found to be −30 Hz.

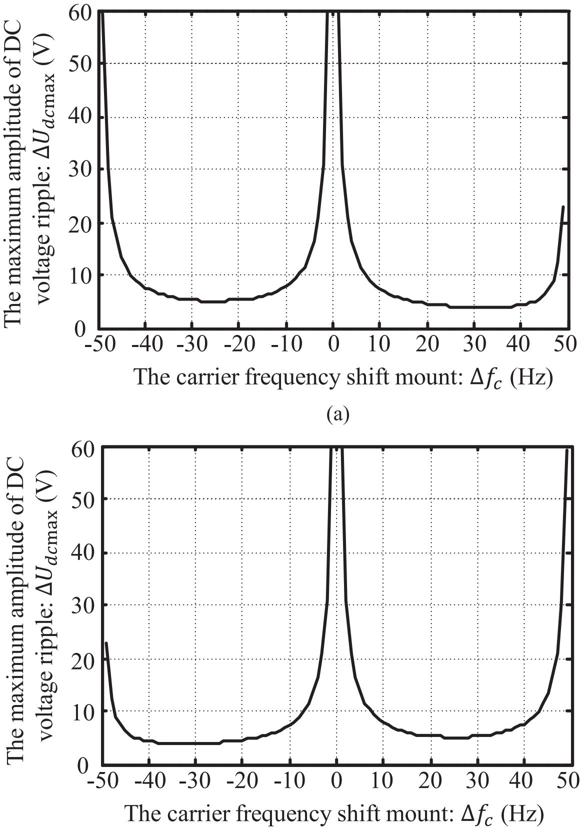

(a)

(b)

Fig. 7. Maximum dc voltage ripple amplitude versus the carrier frequency shift Δf_c. (a): $f_h = 2f_c - f_s$; (b): $f_h = 2f_c + f_s$.

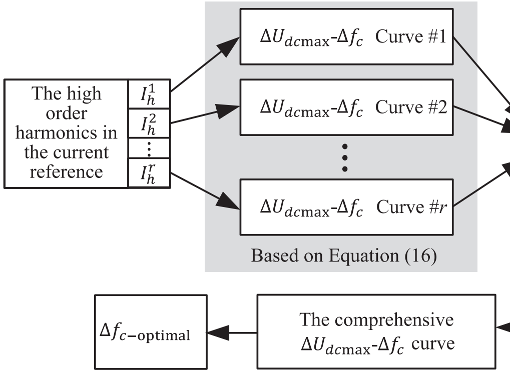

Fig. 8. Proposed ACFO method.

When the CHB-based APF outputs several high-order harmonic currents, the approach to selecting $\Delta f_{c-\mathrm{optimal}}$ is that: draw the $\Delta U_{\mathrm{dcmax}}$–$\Delta f_c$ curve for each harmonic current component, respectively, and superpose them to obtain the overall $\Delta U_{\mathrm{dcmax}}$–$\Delta f_c$ curve, thereby $\Delta f_{c-\mathrm{optimal}}$ can be selected. Fig. 8 shows the flow diagram of the ACFO method to choose the optimal $\Delta f_{c-\mathrm{optimal}}$ for any output current. The inputs of the ACFO method are the amplitude and frequency of each output high-order harmonic current, denoted as I_h^1, I_h^2 $\cdots$ I_h^r. They can be readily obtained from the harmonic current reference extraction algorithm.

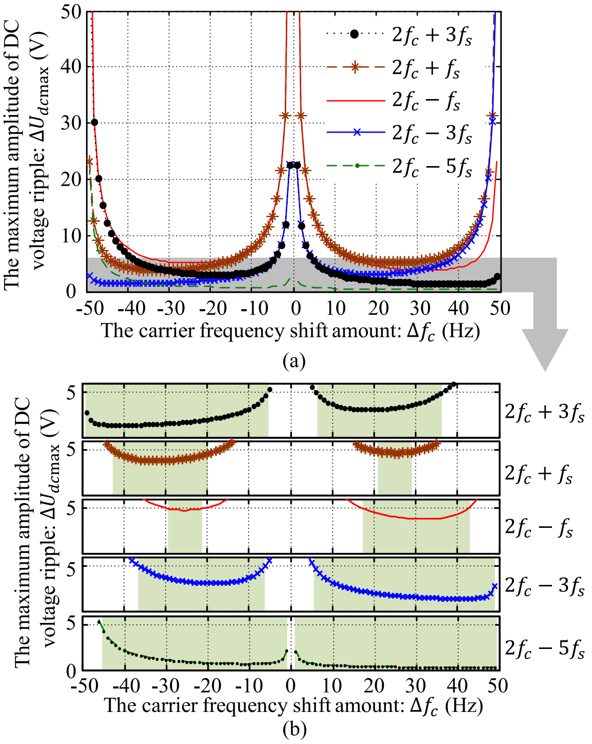

(a)

(b)

Fig. 9. $\Delta U_{\mathrm{dcmax}}$–$\Delta f_c$ curves of harmonic currents at different f_h (a), and the zoom in graph (b).

IV. ANALYSIS AND IMPLEMENTATION OF THE ACFO

A. *Robustness of the ACFO Method*

The proposed ACFO method is an open loop control method. Any nonideal factor, e.g., harmonic detection error, calculation delay and error, will lead to nonoptimized design of $\Delta f_{c\mathrm{-optimal}}$ and nonminimized dc voltage ripple. Therefore, it is necessary to analyze and estimate the robustness of the proposed ACFO method against the deviation of $\Delta f_{c\mathrm{-optimal}}$.

Usually, the switching frequency of a CHB-based APF is several hundred hertz, mostly 600∼800 Hz, thus the first switching harmonic cluster of an H-bridge cell is located at the 19th ∼ 29th harmonic frequency band. While the second switching harmonic cluster of an H-bridge cell is located at a much higher frequency band and with much lower amplitude. As a result, only the HEU problem at the first switching harmonic cluster is of concern. Assume that the amplitude of the output harmonics @$(2f_c+3f_s)$, $(2f_c+f_s)$, $(2f_c-f_s)$, $(2f_c-3f_s)$ and $(2f_c-5f_s)$ are 10 A, respectively; $C = 4500\ \mu$F; $M = 0.75$. According to (16), draw the $\Delta U_{\mathrm{dcmax}}$–$\Delta f_c$ curve of each harmonic current, respectively, the result is illustrated in Fig. 9.

From Fig. 9(a), it is seen that the bottoms of these curves are in a similar flat shape. If the admissible value of $\Delta U_{\mathrm{dcmax}}$ is 5 V for each curve, the selectable regions of Δf_c are shown in Fig. 9(b) and marked by green. From Fig. 9, it is clear that the proposed ACFO method is robust as the dc voltage ripple would not change much when the output harmonic currents change faster than the update of $\Delta f_{c\mathrm{-optimal}}$. Moreover, the minimization of the dc voltage ripple is always acceptable even with a ±5 Hz offset in $\Delta f_{c\mathrm{-optimal}}$.

TABLE II
LOOKUP TABLE FOR ACFO METHOD WHEN $M = 0.75$

Side band order k	Harmonic frequency f_h	Positive optimal $\Delta f_c \Delta f^{+k}_{c\mathrm{-optimal}}$	Negative optimal $\Delta f_c \Delta f^{-k}_{c\mathrm{-optimal}}$	Self-weighting factor W^k_{self}
+5	$2f_c+5f_s$	7 Hz	−47 Hz	0.015
+3	$2f_c+3f_s$	19 Hz	−40 Hz	0.190
+1	$2f_c+1f_s$	25 Hz	−30 Hz	0.529
−1	$2f_c-1f_s$	30 Hz	−25 Hz	0.529
−3	$2f_c-3f_s$	40 Hz	−19 Hz	0.190
−5	$2f_c-5f_s$	47 Hz	−7 Hz	0.015

B. *Engineering Implementation of the ACFO*

The ACFO method shown in Fig. 8 includes the calculation of Bessel functions and a searching process for determining $\Delta f_{c\mathrm{-optimal}}$ based on multiple $\Delta U_{\mathrm{dcmax}}$–$\Delta f_c$ curves. These processes are time-consuming and computation-intensive. In order to simplify the ACFO method and implement it in a CHB-based APF without using a high-cost and high-performance digital controller, a simple engineering implementation of the ACFO based on a lookup table is presented in this section.

It is noted that for a single output harmonic current, the change of current amplitude I_h only influence the amplitude of the corresponding $\Delta U_{\mathrm{dcmax}}$–$\Delta f_c$ curve, but not $\Delta f_{c\mathrm{-optimal}}$. Hence, if the CHB-based APF only outputs one high-order harmonic current, $\Delta f_{c\mathrm{-optimal}}$ is a constant. However usually, several high-order harmonics need to be compensated simultaneously, and the design of $\Delta f_{c\mathrm{-optimal}}$ becomes more complicated and relies on comprehensive $\Delta U_{\mathrm{dcmax}}$–$\Delta f_c$ curves. The idea to simplify the implementation of the ACFO method is to replace the calculation of comprehensive $\Delta U_{\mathrm{dcmax}}$–$\Delta f_c$ curve by simple computation of several $\Delta f_{c\mathrm{-optimal}}$ values. Thus the calculation of Bessel function and the searching process can be avoided.

The $\Delta f_{c\mathrm{-optimal}}$ value of each high-order harmonic frequency can be obtained by corresponding $\Delta U_{\mathrm{dcmax}}$–$\Delta f_c$ curve based on (16) with any current amplitude. Because the $\Delta U_{\mathrm{dcmax}}$–$\Delta f_c$ curve is segmented, both the optimal Δf_c in positive region (denoted as $\Delta f^{+}_{c\mathrm{-optimal}}$) and negative region (denoted as $\Delta f^{-}_{c\mathrm{-optimal}}$) are needed.

The different switching harmonic voltages have different amplitudes, resulting in different degrees of HEU when the harmonic currents have the same amplitude. Therefore, different frequencies should be assigned with different weighting factors based on their switching harmonic amplitudes. According to (4), define the self-weighting factor W^k_{self} as

$$W^k_{\mathrm{self}} = \frac{2\,|a_h|}{\pi U_{\mathrm{dc}}} = \frac{J_k(mM\pi)}{m}. \tag{17}$$

M in (17) is the fundamental modulation index, which is a constant determined by the PCC grid voltage and the designed dc voltage. Assuming $M = 0.75$, the obtained lookup table is shown in Table II. The higher order side-band harmonics with $|k| > 5$ are ignored as their W_{self} are too small (lower than 0.0005) and can be neglected. The lookup table under other modulation index can also be easily obtained by offline calculation based on (16) and (17), and some examples are given in the appendix.

Denote the self-weighting factors in the lookup table as

$$\mathbf{W}_{\mathbf{self}} = \begin{bmatrix} W^{+5}_{\text{self}} & 0 & 0 & 0 & 0 & 0 \\ 0 & W^{+3}_{\text{self}} & 0 & 0 & 0 & 0 \\ 0 & 0 & W^{+1}_{\text{self}} & 0 & 0 & 0 \\ 0 & 0 & 0 & W^{-1}_{\text{self}} & 0 & 0 \\ 0 & 0 & 0 & 0 & W^{-3}_{\text{self}} & 0 \\ 0 & 0 & 0 & 0 & 0 & W^{-5}_{\text{self}} \end{bmatrix}. \tag{18}$$

Divide the six self-weighting factors into two groups as

$$\begin{cases} \mathbf{W}^{+}_{\text{self}} = \left[W^{+5}_{\text{self}},\ W^{+3}_{\text{self}},\ W^{+1}_{\text{self}}\right]^{\mathrm{T}} \\ \mathbf{W}^{-}_{\text{self}} = \left[W^{-1}_{\text{self}},\ W^{-3}_{\text{self}},\ W^{-5}_{\text{self}}\right]^{\mathrm{T}} \end{cases}. \tag{19}$$

Denote the optimal carrier phase shift in the lookup table as (20) in respect to the positive region and negative region respectively,

$$\begin{cases} \mathbf{\Delta f}^{+}_{\text{c-optimal}} = \Delta f^{++5}_{\text{c -optimal}}, \Delta f^{++3}_{\text{c-optimal}}, \Delta f^{++1}_{\text{c-optimal}} \\ \qquad\qquad \Delta f^{+-1}_{\text{c-optimal}}, \Delta f^{+-3}_{\text{c-optimal}},\ \Delta f^{+-5}_{\text{c-optimal}}]^{\mathrm{T}} \\ \mathbf{\Delta f}^{-}_{\text{c-optimal}} = \Delta f^{-+5}_{\text{c -optimal}}, \Delta f^{-+3}_{\text{c-optimal}}, \Delta f^{-+1}_{\text{c-optimal}} \\ \qquad\qquad \Delta f^{--1}_{\text{c-optimal}}, \Delta f^{--3}_{\text{c-optimal}}, \Delta f^{--5}_{\text{c-optimal}}]^{\mathrm{T}}. \end{cases} \tag{20}$$

The harmonic current amplitudes at the six frequencies are obtained from the harmonic current reference extraction algorithm, and are denoted as

$$\mathbf{I_h} = \left[I^{+5}_{h},\ I^{+3}_{h},\ I^{+1}_{h},\ I^{-1}_{h},\ I^{-3}_{h},\ I^{-5}_{h}\right]. \tag{21}$$

Divide $\mathbf{I_h}$ into two groups as

$$\begin{cases} \mathbf{I^{+}_{h}} = \left[I^{+5}_{h},\ I^{+3}_{h},\ I^{+1}_{h}\right] \\ \mathbf{I^{-}_{h}} = \left[I^{-1}_{h},\ I^{-3}_{h},\ I^{-5}_{h}\right] \end{cases}. \tag{22}$$

Thus the weighted optimal Δf_c in the positive region and negative region can be deduced, respectively, as

$$\begin{cases} \Delta f^{+}_{\text{c − optimal}} = \dfrac{\mathbf{I_h W_{self} \Delta f^{+}_{\text{c-optimal}}}}{\text{sum}(\mathbf{I_h W_{self}})} \\ \Delta f^{-}_{\text{c − optimal}} = \dfrac{\mathbf{I_h W_{self} \Delta f^{-}_{\text{c-optimal}}}}{\text{sum}(\mathbf{I_h W_{self}})} \end{cases} \tag{23}$$

where the $sum(\mathbf{I_h W_{self}})$ is the sum of the six elements in $\mathbf{I_h W_{self}}$. Furthermore, the weighting factors of the positive region and negative region are deduced, respectively, as (24), which represent the intensities of HEU in these regions:

$$\begin{cases} W^{+} = \mathbf{I^{+}_{h} W^{+}_{self}} \\ W^{-} = \mathbf{I^{-}_{h} W^{-}_{self}} \end{cases}. \tag{24}$$

If the weighting factor of one region is larger than the other one, the optimal carrier frequency should not be designed in this region. Thus, a logical algorithm to determine which optimal Δf_c should be chosen as the optimal carrier frequency shift is

$$\Delta f_{\text{c−optimal}} = \begin{cases} \Delta f^{-}_{\text{c − optimal}}, W^{+} > W^{-} \\ \Delta f^{+}_{\text{c − optimal}}, W^{+} < W^{-} \end{cases}. \tag{25}$$

The simplified engineering implementation of the ACFO method is shown in Fig. 10.

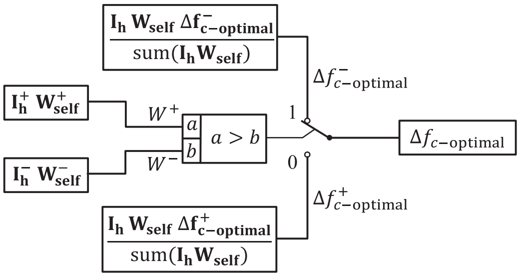

Fig. 10. Simplified engineering implementation of the ACFO method.

TABLE III
PRECISION OF THE SIMPLIFIED ACFO METHOD

Harmonic currents	Original ACFO $\Delta f_{c-\text{optimal}}$	Simplified ACFO $\Delta f_{c-\text{optimal}}$
$I^{-1}_{h} = 10\text{A};\ I^{+1}_{h} = 6\text{A}$	+28.70 Hz	+28.25 Hz
$I^{-3}_{h} = 10\text{A};\ I^{-1}_{h} = 5\text{A}$	+34.92 Hz	+34.18 Hz
$I^{-3}_{h} = 5\text{A};\ I^{+1}_{h} = 8\text{A}$	–26.95 Hz	–27.98 Hz
$I^{-1}_{h} = 5\text{A};\ I^{+1}_{h} = 10\text{A};\ I^{3}_{h} = 5\text{A};$	–29.85 Hz	–29.58 Hz

In summary, the proposed ACFO method consists of three steps, i.e.,

1) offline calculation;
2) storage of lookup table; and
3) online calculation.

The computation burden of each step is evaluated as follows.

1) The purpose of offline calculation is to build up a lookup table as Table II. There are 18 elements to be calculated. Equation (16) is executed six times to obtain $\Delta f^{+k}_{c-\text{optimal}}$ and $\Delta f^{-k}_{c-\text{optimal}}$ (in total 12 elements). Equation (17) is executed six times to obtain W^{k}_{self} (six elements). Since the Bessel functions in (17) have already been calculated in (16), the calculation of (17) only involves one floating-point division. More importantly, this lookup table is solely determined by the modulation index M, whose value will not change during the operation of the CHB-based APF. Therefore, this offline calculation only needs to be executed once during the design stage.
2) Since there are only 18 floating-point numbers to be stored in the lookup table, the occupied memory space in the controller chip is negligible.
3) The purpose of online calculation is to generate the optimal Δf_c for different output conditions, and the whole process shown in Fig. 10 consists of 18 floating-point multiplications, 15 floating-point additions, 2 floating-point divisions, and 1 floating-point comparison. The online calculation can be finished within 40 clock periods in a DSP or 10 clock periods in an FPGA (by asynchronous parallel computing). Moreover, the online calculation is refreshed only if the output current changes.

To verify the accuracy of the simplified engineering implementation of the ACFO method, a comparison with the original ACFO method in Fig. 8 is presented as in Table III. The calculations are done for the case of $M = 0.75$.

Table III shows that the error of the simplified ACFO method is lower than 1 Hz. Considering the robustness of the ACFO

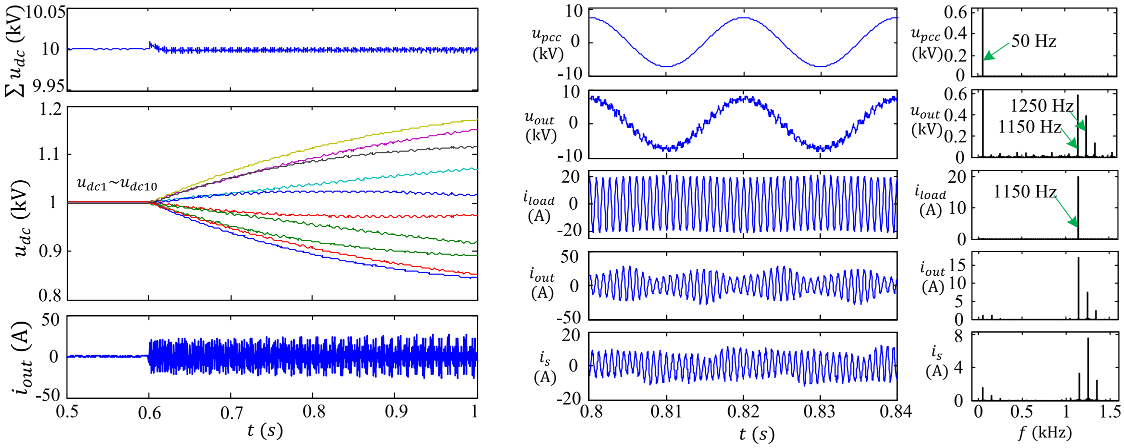

(a) (b)

Fig. 11. Simulation results without ACFO ($f_c = 600$ Hz). (a): DC voltages and output current; (b): AC measurements and their FFT results.

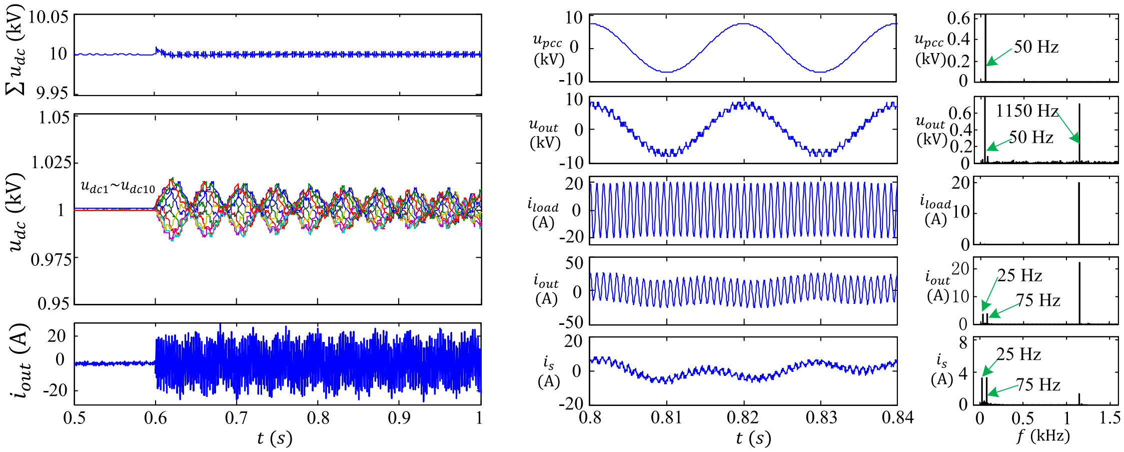

(a) (b)

Fig. 12. Simulation results with modified f_c ($f_c = 612$ Hz). (a): DC voltages and output current; (b): AC measurements and their FFT results.

method discussed above (±5 Hz), the error is acceptable. Thus, the simplified ACFO method is more suitable for engineering implementation without upgrading the hardware of the controller, and a satisfactory precision can be reached.

V. SIMULATION, EXPERIMENT, AND FIELD TEST

A. *Simulation Results*

A single-phase ten-cell-cascaded converter is simulated in PSCAD-EMTDC according to Fig. 2. Other simulation parameters are shown in Table IV. The harmonic load is a 23rd harmonic current source with an amplitude of 20 A and phase of 90°. The current reference of the CHB-based APF is activated at 0.6 s.

The measurements include the dc voltages of all the ten cells $u_{\rm dc1} \sim u_{\rm dc10}$, the overall dc voltage of the CHB chain $\sum u_{\rm dc}$, the CHB output current $i_{\rm out}$, the PCC voltage $u_{\rm pcc}$, the CHB output voltage $u_{\rm out}$, the harmonic load current $i_{\rm load}$, and the grid current i_s. The frequency resolution of the adopted fast Fourier transform (FFT) algorithm is 25 Hz.

TABLE IV
SIMULATION PARAMETERS

Item	value	Item	value
Number of cells per phase	10	Output filter inductance	5 mH
Rated dc voltage of cell	1000 V	Initial carrier frequency	600 Hz
DC capacitor	4500 μF	Carrier phase shift angle	$180°/10$
Capacitor discharge resistor	5000 Ω	Phase voltage of the grid (rms)	5300 V

Fig. 11 shows the simulation result without the ACFO method. Because of the HEU discussed in Section III, the dc voltages start to diverge at 0.6 s, and the unbalanced dc voltages lead to highly distorted output current $i_{\rm out}$. The unbalanced dc voltages can cause 25th and 27th harmonics in the output [22], which are visible from the spectra of $u_{\rm out}$ and $i_{\rm out}$. Consequently, the grid current i_s also contains these harmonics in its spectra.

Fig. 12 shows the simulation result when the carrier frequency is shifted to 612 Hz. The switching harmonic voltage at 1150 Hz,

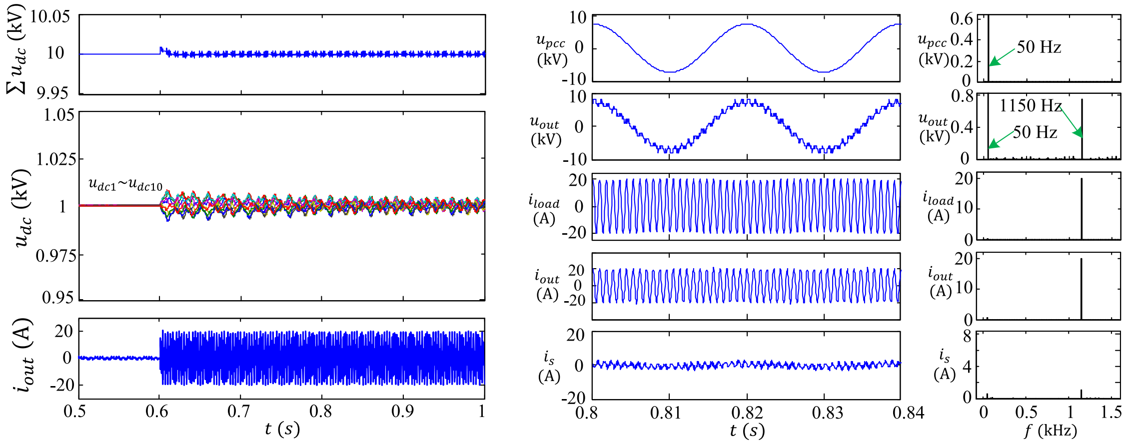

(a) (b)

Fig. 13. Simulation results with ACFO ($f_c = 630$ Hz). (a): DC voltages and output current; (b): AC measurements and their FFT results.

which can cause cell energy unbalance, is shifted to 1175 Hz. From the simulation result, it is seen that after the current reference is added into the current control loop, the dc voltages do not diverge, but have a nearly 25 Hz ripple with an amplitude of about 12 V, which are in good agreement with the theoretical analysis in Section IV. In this case, the output current of CHB-based APF is better than the one in Fig. 11. However, the low-frequency ripples on the dc voltages lead to low frequency distortion of the output current, which can be seen from both the current waveform and its FFT results.

Fig. 13 shows the simulation result when the carrier frequency is shifted to 630 Hz, which is the optimal carrier frequency according to the ACFO method. The switching harmonic voltage at 1150 Hz is shifted to 1210 Hz. After the current reference is added into the current control loop, the dc voltages do not diverge, and the ripple is only about 3 V, which are also in good agreement with the theoretical analysis in Section IV. The spectra of both currents and voltages show that with the ACFO method, the load current is well compensated and only the equivalent switching harmonics are visible in the output spectra of the CHB converter.

B. Experimental Results on a Laboratorial Prototype

The laboratorial prototype shown in Fig. 14 is a single-phase CHB-based APF whose main parameters are shown in Table V. The 200-V MOSFETs are used in the 72-V rated dc voltage cells in order to handle the case of the dc voltage divergence. Without a programmable high-order harmonic current load, the prototype cannot work at the load current compensating mode but the injunctive harmonic current output mode, which means the current reference extraction part in the control system is replaced by a certain harmonic reference. The dc voltages of cell 2, cell 5, and cell 8, and the output current are measured.

First, the output current reference is set to switch from 0 to 23rd harmonic with an amplitude of 5 A. When the carrier frequency is 600 Hz, the typical HEU-induced dc voltage divergence occurs after enabling the harmonic current compensation, as shown in Fig. 15. The unbalanced dc voltages introduce more harmonics to the APF output and make the compensation current distorted. When the proposed ACFO method is adopted, the results are shown in Fig. 16. According to the proposed ACFO method, 630 Hz is the optimal carrier frequency when outputting 23rd order harmonic. Due to the effect of ACFO, the divergence of dc voltages is avoided, furthermore, the dc voltage ripple is minimized to be below 5 V, which makes the output current waveform much better than the one in Fig. 15. Both Figs. 15 and 16 are in good agreement with the simulation results.

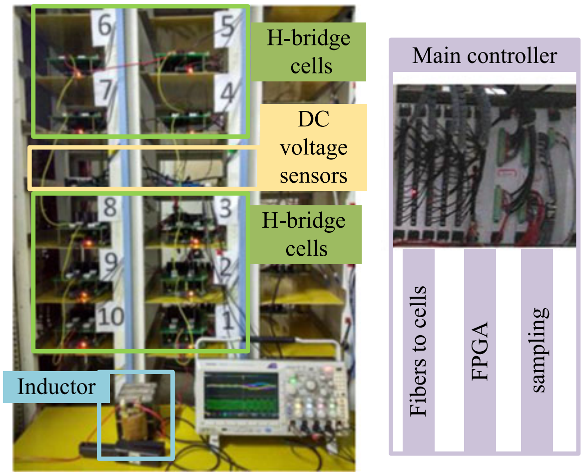

Fig. 14. Laboratorial prototype of a ten-cell-cascaded single-phase APF.

TABLE V
SINGLE PHASE CHB-BASED APF PROTOTYPE PARAMETERS

Item	value	Item	value
Number of H-bridge cells	10	Initial carrier frequency	600 Hz
Rated dc voltage of cell	72 V	Carrier phase shift angle	$180°/10$
DC capacitor	2720 μF	Phase voltage of the grid (rms)	380 V
Capacitor discharge resistor	3000 Ω	Rated modulation index	0.75
Output filter inductance	1 mH	Switch model	IRFS4227Pbf

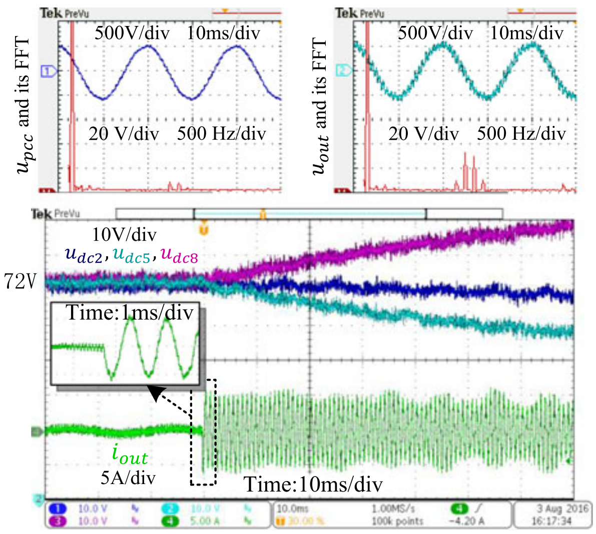

Fig. 15. HEU-induced dc voltage divergence.

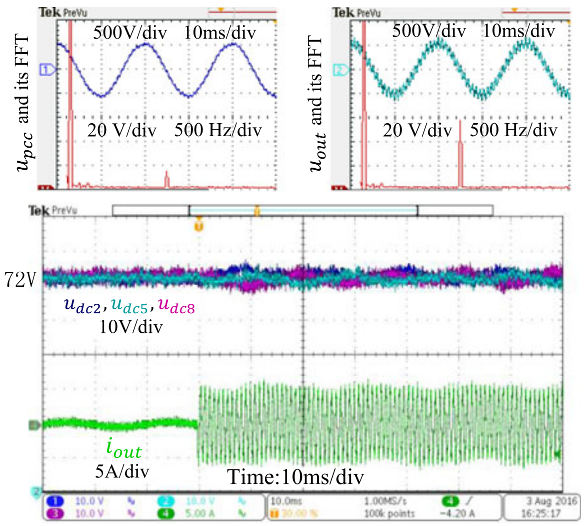

Fig. 16. Effectiveness of proposed ACFO method.

Two different current references are set to further test the dynamic performance of the proposed ACFO method. The first harmonic reference is a 21st harmonic with 5 A amplitude, whose optimal carrier frequency is 640 Hz. The second harmonic reference consists of a 25th harmonic with 2 A amplitude and a 27th harmonic with 5 A amplitude, whose optimal carrier frequency is 565.3 Hz. Fig. 17 shows the measured waveforms with the carrier frequency kept at 640 Hz. When the output current only contains 21st harmonic, the dc voltages are well regulated, but when the output current changes, the dc voltages obviously contain low-frequency ripples. This reveals that the simple noninteger ratio carrier frequency modulation method is not adequate for the complex operation conditions of the CHB-based APF.

Fig. 18 shows the result when the proposed ACFO method is adopted for the same testing condition as in Fig. 17. The dc voltages can always be balanced with minimized dc ripple due to the self-adaptability of the proposed ACFO method. The current waveform is not significantly improved as the voltage variation of cell capacitors in Fig. 17 is only 5 V or 6.9% of the nominal dc capacitor voltage, which can be easily compensated by a fast current control loop.

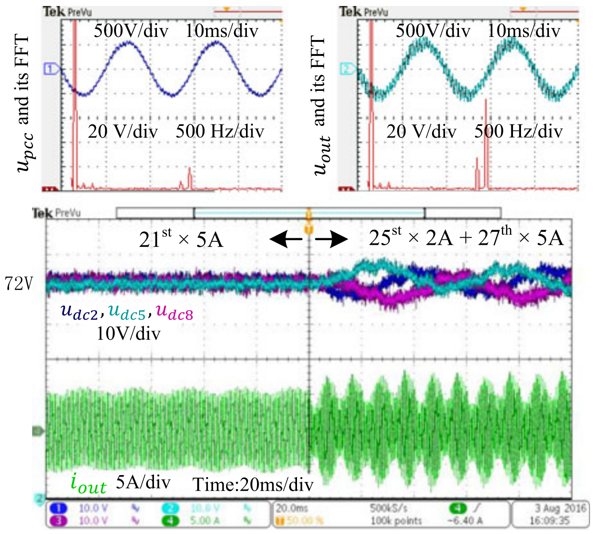

Fig. 17. Dynamic performance of simple noninteger ratio carrier frequecny modulation.

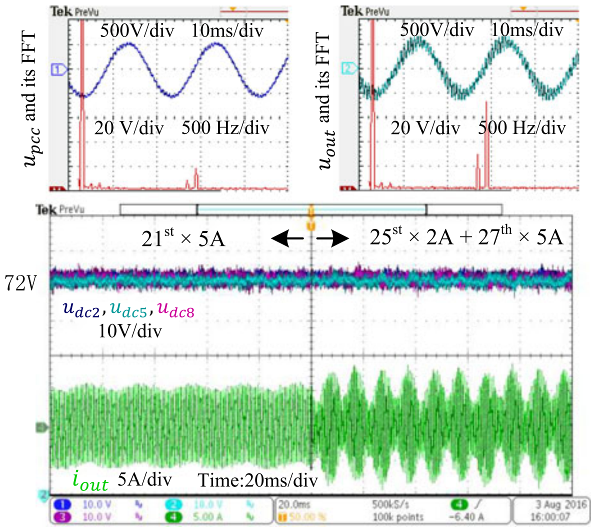

Fig. 18. Dynamic performance of proposed ACFO method.

C. Field Test Results

The industrial filed test of the carrier frequency optimization method proposed in this paper was done in an 8 MVA, 35 kV, 36-cell-cascaded power quality compensator (see Fig. 19), whose topology is the same as Fig. 2. Fig. 20 is the measured FFT result of the PCC voltage, which shows that 23rd and 25th harmonic pollution was serious. The CHB-based power quality compensator operated at the carrier frequency of 600 Hz. The main switching harmonic voltages of the cell at $(2f_C \pm f_s)$ were exactly 23rd and 25th harmonics, thus the converter suffered from

Fig. 19. ±8MVA, 35 kV, 36-cell-cascaded power quality compensator.

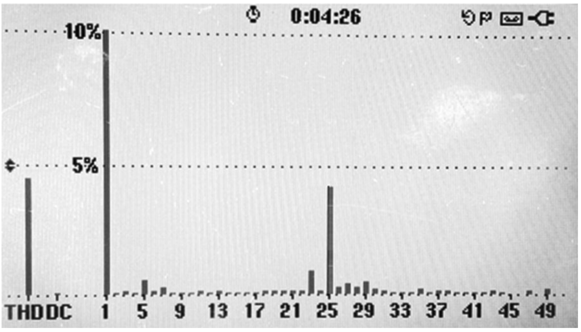

Fig. 20. FFT analysis of the 35 kV PCC voltage.

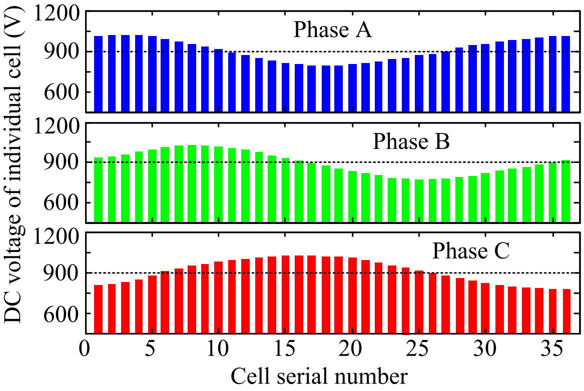

Fig. 21. DC voltages of each cell without ACFO, $f_C = 600$ Hz.

a serious HEU if harmonic current with same frequencies need to be compensated by this CHB-based APF. Fig. 21 shows the dc voltages of all cells after the device was put into operation for several seconds. The dc voltages started to oscillate and this phenomenon shows good agreement with the theoretical analysis in Fig. 5. Because of the quick divergence of dc voltages, the converter could not work normally, and component damage occurred from time to time. Due to limited measurement environment and project confidentiality, further detail data are not presented.

To deal with this HEU-induced problem, the proposed ACFO method was adopted. Fig. 22 shows the dc voltages of all cells after the equipment was put into operation. It is clear that the dc voltages are balanced and well regulated, which verifies the effectiveness of the proposed method.

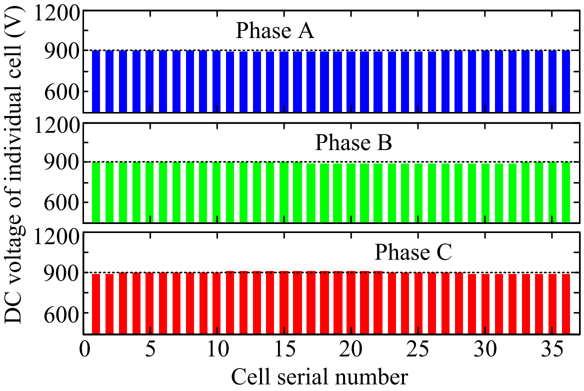

Fig. 22. DC voltages of each cell with ACFO, $f_C = 576$ Hz.

VI. CONCLUSION

1) In this paper, the HEU phenomenon in a CHB-based APF with CPS-PWM has been revealed, which is the main reason of dc voltage unbalance and divergence when the APF compensates high-order harmonics. Meanwhile, the mechanism analysis shows that this type of unbalance harmonic energy exchange is caused by the coupling of output harmonic current and switching harmonic voltages of each cell.
2) To overcome this problem, this paper has proposed an ACFO method. As the carrier frequency can essentially influence the harmonic energy exchange, the impact on dc voltages of HEU under different carrier frequencies can be predicted and plotted as a $\Delta U_{\mathrm{dcmax}}$–$\Delta f_c$ curve. From the curve, the ACFO method can adaptively select the optimal carrier frequency according to the output of the APF, which not only avoids the HEU-induced dc voltage divergence but also minimizes the dc voltage ripples. However, the original ACFO method is computation-intensive and resource-demanding, and a simplified implementation of ACFO is developed further, which replaces the complicated nonlinear calculations and search process by a simple linear operation and a small size lookup table built offline. Because of the low calculation demand and satisfactory precision, this simplified engineering implementation of the ACFO can be widely used in an existing CHB-based APF a without high performance hardware controller.
3) Although the simple noninteger ratio carrier frequency modulation can also avoid HEU-induced divergence of the dc voltages, it cannot avoid the high-amplitude low-frequency ripple on the dc voltage, which can affect the regulation of the APF output current and the lifetime of dc capacitors. In order to ensure the proper control of a CHB-based APF in uncertain and complicated operation conditions, ACFO is a simple and effective method, and it has been verified by simulations, experiments and field tests.

APPENDIX

TABLE VI
LOOKUP TABLE FOR ACFO METHOD WHEN $M = 0.8$

Side band order k	Harmonic frequency f_h	Positive optimal $\Delta f_c \Delta f^{+k}_{c\text{-optimal}}$	Negative optimal $\Delta f_c \Delta f^{-k}_{c\text{-optimal}}$	Self-weighting factor W^k_{self}
$+5$	$2f_c + 5f_s$	10 Hz	–46 Hz	0.022
$+3$	$2f_c + 3f_s$	20 Hz	–40 Hz	0.219
$+1$	$2f_c + 1f_s$	25 Hz	–31 Hz	0.494
–1	$2f_c - 1f_s$	31 Hz	–25 Hz	0.494
–3	$2f_c - 3f_s$	40 Hz	–20 Hz	0.219
–5	$2f_c - 5f_s$	46 Hz	–10 Hz	0.022

TABLE VII
LOOKUP TABLE FOR ACFO METHOD WHEN $M = 0.9$

Side band order k	Harmonic frequency f_h	Positive optimal $\Delta f_c \Delta f^{+k}_{c\text{-optimal}}$	Negative optimal $\Delta f_c \Delta f^{-k}_{c\text{-optimal}}$	Self-weighting factor W^k_{self}
$+5$	$2f_c + 5f_s$	12 Hz	–45 Hz	0.033
$+3$	$2f_c + 3f_s$	23 Hz	–38 Hz	0.278
$+1$	$2f_c + 1f_s$	25.5 Hz	–28 Hz	0.401
–1	$2f_c - 1f_s$	28 Hz	–25.5Hz	0.401
–3	$2f_c - 3f_s$	38 Hz	–23 Hz	0.278
–5	$2f_c - 5f_s$	45 Hz	–12 Hz	0.033

REFERENCES

[1] G. Carlos, C. Jacobina, E. Santos, E. Fabricio, and N. Rocha, "Shunt active power filter with open-end winding transformer and series-connected converters," *IEEE Trans. Ind. Appl.*, vol. 51, no. 4, pp. 3273–3283, Jul. /Aug. 2015.

[2] Y. Deng, X. Tong, and H. Jia, "A bidirectional control principle of active tuned hybrid power filter based on the active reactor using active techniques," *IEEE Trans. Ind. Informat.*, vol. 11, no. 1, pp. 141–154, Feb. 2015.

[3] C. S. Lam, M. C. Wong, W. H. Choi, X. X. Cui, H. M. Mei, and J. Z. Liu, "Design and performance of an adaptive low-DC-voltage-controlled LC-hybrid active power filter with a neutral inductor in three-phase four-wire power systems," *IEEE Trans. Ind. Electron.*, vol. 61, no. 6, pp. 2635–2647, Jun. 2014.

[4] T. Lee, Y. Wang, J. Li, and J. Guerrero, "Hybrid active filter with variable conductance for harmonic resonance suppression in industrial power systems," *IEEE Trans. Ind. Electron.*, vol. 62, no. 2, pp. 746–756, Feb. 2015.

[5] S. Rahmani, A. Hamadi, K. Al-Haddad, and L. A. Dessaint, "A combination of shunt hybrid power filter and thyristor-controlled reactor for power quality," *IEEE Trans. Ind. Electron.*, vol. 61, no. 5, pp. 2152–2164, May 2014.

[6] Z. Chen, Y. Luo, and M. Chen, "Control and performance of a cascaded shunt active power filter for aircraft electric power system," *IEEE Trans. Ind. Electron.*, vol. 59, no. 9, pp. 3614–3623, Sep. 2012.

[7] M. E. Ortuzar, R. E. Carmi, J. W. Dixon, and L. Moran, "Voltage-source active power filter based on multilevel converter and ultracapacitor DC link," *IEEE Trans. Ind. Electron.*, vol. 53, no. 2, pp. 477–485, Apr. 2006.

[8] A. K. Panda and S. S. Patnaik, "Analysis of cascaded multilevel inverters for active harmonic filtering in distribution networks," *Int. J. Elect. Power Energy Syst.*, vol. 66, pp. 216–226, Mar. 2015.

[9] J. A. Munoz, J. R. Espinoza, C. R. Baier, L. A. Morán, J. I. Guzmán, and V. M. Cárdenas, "Decoupled and modular harmonic compensation for multilevel STATCOMs," *IEEE Trans. Ind. Electron.*, vol. 61, no. 6, pp. 2743–2753, Jun. 2014.

[10] B. Sangeetha and K. Geetha, "Performance of multilevel shunt active filter for smart grid applications," *Int. J. Elect. Power Energy Syst.*, vol. 63, pp. 927–932, Dec. 2014.

[11] A. Valdez-Fernandez, P. Martinez-Rodriguez, G. Escobar, C. Limones-Pozos, and J. Sosa, "A model-based controller for the cascade H-bridge multilevel converter used as a shunt active filter," *IEEE Trans. Ind. Electron.*, vol. 60, no. 11, pp. 5019–5028, Nov. 2013.

[12] M. R. Miveh, M. F. Rahmat, A. A. Ghadimi, and M. W. Mustafa, "Power quality improvement in autonomous microgrids using multi-functional voltage source inverters: A comprehensive review," *J. Power Electron.*, vol. 15, no. 4, pp. 1054–1065, Jul. 2015.

[13] V. Khadkikar, "Enhancing electric power quality using UPQC: A comprehensive overview," *IEEE Trans. Power Electron.*, vol. 27, no. 5, pp. 2284–2297, May 2012.

[14] T. Mannen and H. Fujita, "Dynamic control and analysis of dc-capacitor voltage fluctuations in three-phase active power filters," *IEEE Trans. Power Electron.*, vol. 31, no. 9, pp. 6710–6718, Sep. 2016.

[15] R. Ribeiro, T. Rocha, R. Sousa, E. Santos, and A. Lima, "A robust dc-link voltage control strategy to enhance the performance of shunt active power filters without harmonic detection schemes," *IEEE Trans. Ind. Electron.*, vol. 62, no. 2, pp. 803–813, Feb. 2015.

[16] G. Buticchi, D. Barater, E. Lorenzani, C. Concari, and G. Franceschini, "A nine-level grid-connected converter topology for single-phase transformerless PV systems," *IEEE Trans. Ind. Electron.*, vol. 61, no. 8, pp. 3951–3960, Aug. 2014.

[17] D. Sreenivasarao, P. Agarwal, and B. Das, "Performance evaluation of carrier rotation strategy in level-shifted pulse-width modulation technique," *IET Power Electron.*, vol. 7, no. 3, pp. 667–680, Mar. 2014.

[18] E. Behrouzian, M. Bongiorno, and R. Teodorescu, "Impact of switching harmonics on capacitor cells balancing in phase-shifted PWM based cascaded H-bridge STATCOM," *IEEE Trans. Power Electron.*, vol. 32, no. 1, pp. 815–824, Jan. 2017.

[19] K. Ilves, L. Harnefors, S. Norrga, and H. Nee, "Analysis and operation of modular multilevel converters with phase-shifted carrier PWM," *IEEE Trans. Power Electron.*, vol. 30, no. 1, pp. 268–283, Jan. 2015.

[20] Y. Tang, F. Blaabjerg, P. C. Loh, C. Jin, and P. Wang, "Decoupling of fluctuating power in single-phase systems through a symmetrical half-bridge circuit," *IEEE Trans. Power Electron.*, vol. 30, no. 4, pp. 1855–1865, Apr. 2015.

[21] G. Farivar, B. Hredzak, and V. Agelidis, "Decoupled control system for cascaded h-bridge multilevel converter based STATCOM," *IEEE Trans. Ind. Electron.*, vol. 63, no. 1, pp. 322–331, Jan. 2016.

[22] J. Barrena, L. Marroyo, M. M. Vidal, and J. Apraiz, "Individual voltage balancing strategy for PWM cascaded H-bridge converter-based STATCOM," *IEEE Trans. Ind. Electron.*, vol. 55, no. 1, pp. 21–29, Jan. 2008.

[23] Z. Liu, B. Liu, S. Duan, and Y. Kang, "A novel dc capacitor voltage balance control method for cascade multilevel STATCOM," *IEEE Trans. Power. Electron.*, vol. 27, no. 1, pp. 14–27, Jan. 2012.

[24] D. G. Holmes and T. A. Lipo, *Pulse Width Modulation for Power Converters: Principles and Practice* (Series on Power Engineering). Piscataway, NJ, USA: IEEE Press, 2003, ch. 5.

[25] K. Ilves, L. Harnefors, S. Norrga, and H. Nee, "Predictive sorting algorithm for modular multilevel converters minimizing the spread in the submodule capacitor voltages," *IEEE Trans. Power. Electron.*, vol. 30, no. 1, pp. 440–449, Jan. 2015.

[26] C. D. Townsend, T. J. Summers, J. Vodden, A. J. Watson, R. E. Betz, and J. C. Clare, "Optimization of switching losses and capacitor voltage ripple using model predictive control of a cascaded h-bridge multilevel statcom," *IEEE Trans. Power. Electron.*, vol. 28, no. 7, pp. 3077–3087, Jul. 2013.

[27] S. Bifaretti, L. Tarisciotti, A. Watson, P. Zanchetta, A. Bellini, and J. Clare, "Distributed commutations pulse-width modulation technique for high-power AC/DC multi-level converters," *IET Power Electron.*, vol. 5, no. 6, pp. 909–919, Jul. 2011.

[28] L. Tarisciotti, P. Zanchetta, A. Watson, S. Bifaretti, J. C. Clare, and P. W. Wheeler, "Active DC voltage balancing PWM technique for high-power cascaded multilevel converters," *IEEE Trans. Ind. Electron.*, vol. 61, no. 11, pp. 6157–6167, Nov. 2014.

[29] S. Fan, K. Zhang, J. Xiong, and Y. Xue, "An improved control system for modular multilevel converters with new modulation strategy and voltage balancing control," *IEEE Trans. Power. Electron.*, vol. 30, no. 1, pp. 358–371, Jan. 2015.

[30] M. Alvarenga and J. Pomilio, "Voltage balancing and commutation suppression in symmetrical cascade multilevel converters for power quality applications," *IEEE Trans. Ind. Electron.*, vol. 61, no. 11, pp. 5996–6003, Nov. 2014.

[31] A. Marzoughi and H. Imaneini, "Optimal selective harmonic elimination for cascaded H-bridge-based multilevel rectifiers," *IET Power Electron.*, vol. 7, no. 2, pp. 350–356, Feb. 2014.

[32] IEC 61000-3-6 Assessment of emission limits for distorting loads in MV and HV power systems-Basic EMC publication, Oct. 1996.

[33] W. Bin, *High Power Converters and AC Drives*. New York, NY, USA: Wiley, 2006.

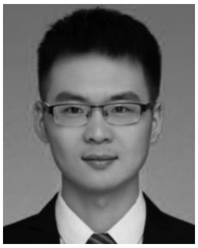

Zezhou Yang (S'15) was born in 1990. He received the B.Eng. degree in electrical engineering and automation from Wuhan University, Wuhan, China, in 2013. He is currently working toward the Ph.D. degree in electrical engineering at Wuhan University, Hubei, China.

His current research interests include multilevel converters, multicarrier modulation techniques, and power quality analysis and control.

Jianjun Sun (M'13) was born in 1975. He received the B.Eng. degree in electrical engineering from Wuhan University of Hydraulic and Electrical Engineering, Wuhan, China, in 1997, and the M.Eng. and Ph.D. degrees in electrical engineering from Wuhan University, Wuhan, China, in 2000 and 2007, respectively.

He is curretly with the School of electrical engineering, Wuhan University as an Associate Professor and the Deputy Director of the Motor and Power Electronics Center. His current research interests include modeling and analysis of high-power power-electronic system, operation and control of microgrid, and power quality analysis and compensation.

Dr. Sun is also an Associate Director of Wuhan power supply society.

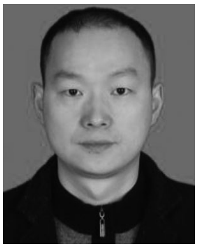

Shangsheng Li (M'13) received the B.Eng., M.Eng., and Ph.D. degrees in electrical engineering from Wuhan University, Wuhan, China, in 2004, 2006, and 2016, respectively.

He is currently with the School of Electrical Engineering, Wuhan University. His research interests include high-power converters such as static synchronous compensators, active power filters, and high-power experimental source techniques.

Meng Huang (S'11–M'13) received the B.Eng. and M.Eng. degrees in electronic science and technology from Huazhong University of Science and Technology, Wuhan, China, in 2006 and 2008, respectively, and the Ph.D. degree in power electronics from the Hong Kong Polytechnic University, Hong Kong, in 2013.

He is currently an Associate Professor of the School of Electrical Engineering, Wuhan University, Wuhan, China. His research interests include nonlinear analysis of power converters and power electronics reliability.

Xiaoming Zha (M'02) was born in Huaining, Anhui Province, China, in 1967. He received B.S., M.S., and Ph.D. degrees in electrical engineering from Wuhan University, Wuhan, China, in 1989, 1992, and 2001.

He was a Postdoctoral Fellow at the University of Alberta, Canada from 2001 to 2003. He has been a Faculty Member of Wuhan University since 1992, and became a Professor in 2003. He is currently the Deputy Dean in the school of electrical engineering, Wuhan University, Wuhan, China. His research interests include power electronic converter, the application of power electronics in smart grid and renewable energy generation, the analysis and control of microgrid, the analysis and control of power quality, and frequency control of high-voltage high-power electric motors.

Yi Tang (S'10–M'14) received the B.Eng. degrees in electrical engineering from Wuhan University, Wuhan China in 2007 and the M.Sc. and Ph.D. degrees from the School of Electrical and Electronic Engineering, Nanyang Technological University, Singapore, in 2008 and 2011, respectively.

From 2011 to 2013, he was a Senior Application Engineer with Infineon Technologies Asia Pacific, Singapore. From 2013 to 2015, he was a Postdoctoral Research Fellow with Aalborg University, Aalborg, Denmark. Since March 2015, he has been with Nanyang Technological University, Singapore as an Assistant Professor. He is the Cluster Director in advanced power electronics research program in the Energy Research Institute, Nanyang Technological University (ERI@N).

Dr. Tang serves as an Associate Editor of the IEEE JOURNAL OF EMERGING AND SELECTED TOPICS IN POWER ELECTRONICS. He received the Infineon Top Inventor Award in 2012.